12-11-2019

Monte Carlo and Experimental Analysis of a Novel Directional Rotating Scatter Mask Gamma Detection System

Julie V. Logan
Massachusetts Institute of Technology

Darren E. Holland
Cedarville University

Larry W. Burggraf
Air Force Institute of Technology

Justin A. Clinton
Air Force Institute of Technology

Buckley E. O'Day III
Air Force Institute of Technology

Recommended Citation

Logan, J. V, Holland, D. E., Burggraf, L. W., Clinton, J. A., & O'Day, B. E. (2019). Monte Carlo and experimental analysis of a novel directional rotating scatter mask gamma detection system. Nuclear Instruments and Methods in Physics Research Section A: Accelerators, Spectrometers, Detectors and Associated Equipment, 947(11 Dec), 162698. https://doi.org/10.1016/j.nima.2019.162698

Version of Record: https://www.sciencedirect.com/science/article/pii/S0168900219311696
Manuscript_46b0080a0ec21d8373eda3f98a1f687f

Monte Carlo and Experimental Analysis of a Novel Directional Rotating Scatter Mask Gamma Detection System

Julie V. Logan[a,b], Darren E. Holland[c], Larry W. Burggraf[a], Justin A. Clinton[a], Buckley E. ODay III[a,1,]

[a] *Department of Engineering Physics at the Air Force Institute of Technology, WPAFB, OH.*
[b] *Department of Nuclear Science and Engineering at Massachusetts Institute of Technology Cambridge, MA.*
[c] *Department of Engineering and Computer Science at Cedarville University, Cedarville, OH.*

Abstract

For such diverse applications as on-site radiation monitoring, treaty or material verification, cargo monitoring during transport, and orphan source location a radioactive source localization system is of great use. The Rotating Scatter Mask (RSM) detection system, a rapid scatter mask retrofit to a conventional radiation detector, provides a low-cost, large field of view and energy range solution to this problem. This work demonstrates successful experimental operation of a prototype system to identify source direction which was modeled using a library of signals simulated using GEANT and a novel algorithm, validated by comparing results with MCNP and experiment.

Keywords: Gamma-ray detection, rotating scatter mask (RSM), scintillators, radioactive source imaging, GEANT, Monte-Carlo simulation

1. Introduction

Due to their widespread use in medicine, industry, agriculture, and research in virtually all countries around the world, sealed radioactive sources (SRSs) have the potential to be abandoned, lost, stolen, or transferred without authorization. These orphan sources are a large-scale problem as the total worldwide inventory of SRSs is estimated to be in the millions and many sources contain concentrations of radionuclides in the GBq to PBq range. Serious and life-threatening incidents have been reported in association with lost SRSs. [1] Rapid identification of an orphan radioactive source is essential in order to minimize the population risk associated with these sources. [2] In accomplishing this goal, directionally-sensitive radiation detectors have been shown to provide a substantial improvement in search efficiency over non-imaging standard radiation detectors. [3] Additional applications of such

Email addresses: jvl2xv@mit.edu (Julie V. Logan), (dholland@cedarville.edu (Darren E. Holland), Larry.Burggraf@afit.edu (Larry W. Burggraf), (Justin.Clinton@afit.edu (Justin A. Clinton), boday@afit.edu (Buckley E. ODay III)

a detection system include, but are not limited to, fixed site radiation monitoring, treaty or material verification, and cargo monitoring during transport.

Extant alternative imaging detectors that provide source location information are each challenged in one or more of the following ways: limited detector field of view, applicability only to photon energies where Compton scatter is the dominant interaction process, or cost. Stationary coded aperture based imagers are subject to the first and third limitations. [4] [5] Rotation modulation technologies are subject to the first limitation. [6] [7] Applications dependent on Compton camera techniques are largely hindered by the second. [8] [9] The rotating scatter mask (RSM) detection system modeled in this effort has a nearly 4π field of view only somewhat limited in forward and backward directions relative to mask rotation, functions in a broad energy regime (from hundreds of keV to multi-MeV photons), and is relatively low cost.

2. The Rotating Scatter Mask Detection System

2.1. Scattering Mask Design

In designing a mask for high accuracy imaging, one would like it to possess the following three traits: first, the total mass presented between the source and detector for a single complete RSM rotation is similar for any source direction; second, the mass between the source and detector during a RSM rotation changes with the rotational angle; and third, the change in the mass between the source and detector varies smoothly during a RSM rotation. The first property ensures the detector response is not biased against any source direction; it should see all source directions equally well. The second property is important because the probability that a photon will pass without interaction from the source to the detector depends on the presence of intervening material. Thus, with RSM rotation, a continually varying mass will attenuate incident gammas accordingly and allow use of the full energy peak (FEP) counts to determine source direction. The third property enhances accuracy because a smoothly varying mass leads to smoothly varying and more distinguishable experimental FEP detector response curves (DRC) which can be compared against a library of simulation DRCs to determine source location [10]. This design concept was presented by FitzGerald in 2015 and one variant of the resulting geometry is presented in Fig. (1). This design ensures that, for each polar angle ϕ, the amount of mass present between the photon source and the center of the detector at any moment during mask rotation varies uniquely as a function of azimuthal rotation angle θ. Thus, the detector provides a unique FEP DRC that depends on the source location relative to the detector position. [11]

A spherical coordinate system is utilized in this analysis, with theta indicating the azimuthal angle and phi indicating the polar angle. An angle (θ,ϕ) specifies a vector pointing from the center of the detector, the origin of the coordinate system, to a potential source position in 4π. The mask rotates 360° in azimuthal angle θ. The definition of the coordinate system with respect to the mask geometry is found in Fig. (1). Computational work has been conducted to optimize this design further to achieve the highest possible source position determination resolution [12], but this experimental effort utilizes the original design as a proof of principle. Throughout its rotation, the detector is tracking the energy spectrum

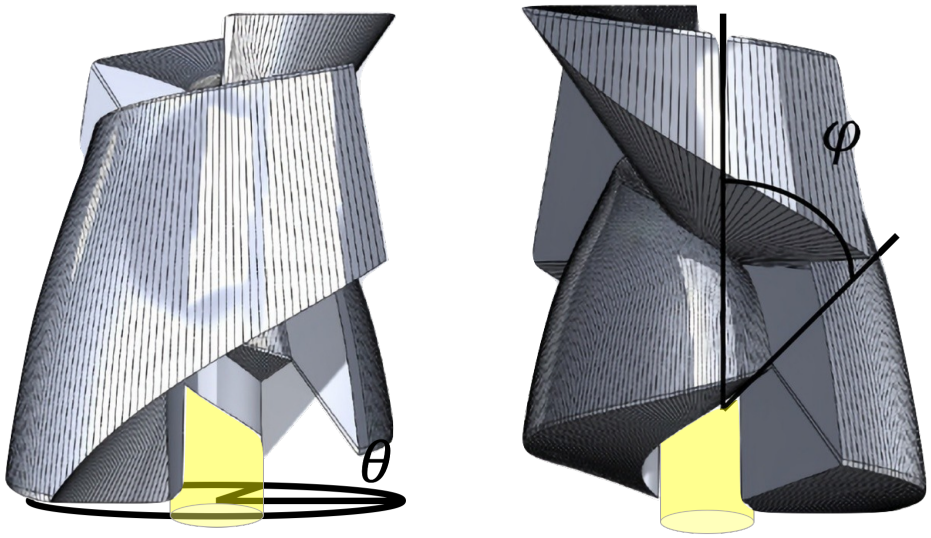

Figure 1: Visualization of rotating scatter mask geometrical design. Polar coordinate, ϕ, and azimuthal coordinate, θ, are also shown. The mask rotates in θ and a source can be offset from the Z axis by an angle ϕ. The detector is positioned in a cylindrical cavity in the center of the mask and is shown in yellow.

associated with each discretized azimuthal angle of mask rotation. This discretization is 5° in θ within the simulation and $2.78° \times 10^{-5}$ in the experiment. The experimental data is subsequently binned to achieve discretization equivalent to the simulation discretization (for ease of comparison). If one produces a cumulative sum of the counts within the full energy peak (FEP) for each azimuthal angle and graphs it as a function of the azimuthal angle θ, one obtains a detector response curve (DRC). This curve is unique to each (θ,ϕ) potential source vector with respect to the stationary detector. The unique nature of this DRC forms the foundation of the imaging ability of the RSM system.

2.2. Simulated System

A proposed RSM system is modeled in both MCNP6 and GEANT4. These simulations are essential for efficient production of a library of DRCs that can be employed in the source localization algorithm. Validated simulations conducted in this effort also form the foundation for further mask design optimization and accurate uncertainty quantification [12]. The scattering mask geometry was defined within a Computer-Aided Design (CAD) file, and subsequently meshed into 91,817 individual tetrahedra to approximate the smooth curvature of the mask. To import the CAD model into MCNP, the Atilla software package is used to create an unstructured mesh. The scattering mask is modeled as poly(methyl methacrylate) (PMMA) with a density of 1.19 g/cc, while the NaI detector was modeled as a 7.62 x 7.62 cm right circular cylinder surrounded by a thin 2024 Al alloy casing. Identical volumes, materials, and sources are defined in both transport codes. All simulations use a 662 keV gamma point source placed at 86.36 cm from the center of the detector. For

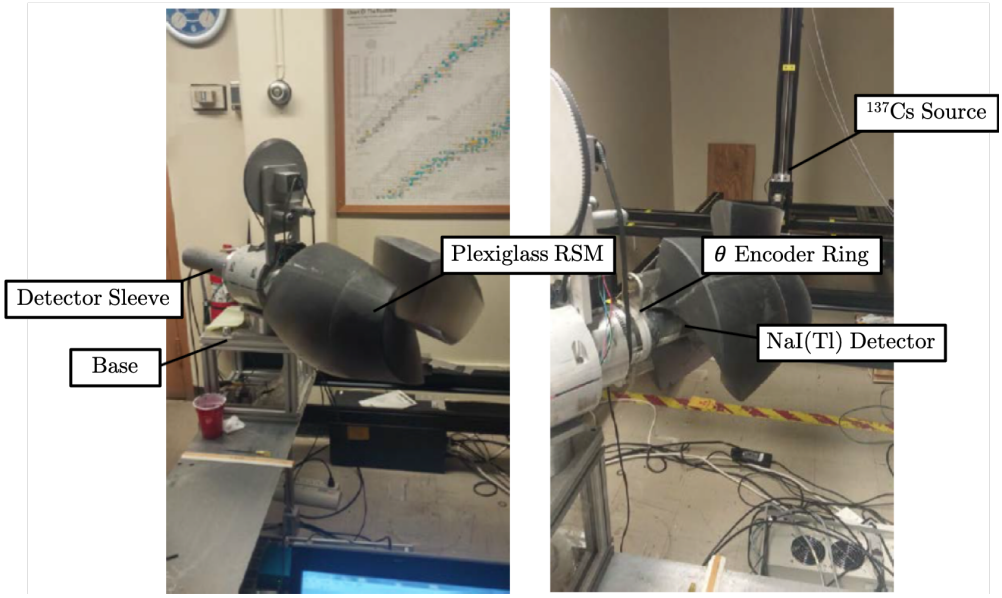

Figure 2: Operational prototype system of the RSM, consisting primarily of a NaI(Tl) detector embedded within a PMMA (plexiglass) mask constructed using polymer printing additive manufacture.

computational efficiency, the isotropic point-source is implemented as an incident conical beam with a 17.5° half-angle of spread which completely encompassed the RSM assembly geometry. Rotation of the mask in the transport codes is obtained through rotation of the source around a stationary mask, as the relative motion is identical to that achieved experimentally.

2.3. Experimental System

Experimentally, the rotating scatter mask detector consists of all components shown in Fig. (2). This primarily consists of a 3" x 3" NaI(Tl) scintillating detector embedded within a specially designed PMMA mask. This mask can be entirely contained within a 0.045 m^3 cube (side length of 35.56 cm). The assembly is placed on a Velmex 4800 Series Rotary Table with a 2-phase 1.8°/step Vexta Stepping Motor. The detector is surrounded by a thin aluminum alloy sleeve of thickness 0.3175 cm to support the mask weight. The mask is rotated via a stepping motor system, as shown in Fig. (2), at a rate of approximately 3°/sec.

A 1.045 mCi ^{137}Cs source is positioned at a constant Z coordinate of 86.36 cm from the center of the NaI(Tl) detector (in order to make valid the use of the point source approximation). This distance is maintained as, for each individual 24 hour run, the source is positioned in a direction associated with each 10° increment of phi (ϕ=5° to 175°). The mask rotation angle reader inherently outputs with resolution of $2.78° \times 10^{-5}$, which is subsequently binned into 5° increments in θ, for comparison with the simulations.

Table 1: P-values associated with the application of the Anderson-Darling k-sample test and the Kolmogorov-Smirnov test in comparing the MCNP and GEANT4 energy spectra for four mask positions. All P-values indicate that, statistically, the distributions could have been sampled from the same set, as one fails to reject the null hypothesis.

Test	(90°, 90°)	(90°, 45°)	(45°, 90°)	(45°, 45°)
Anderson-Darling P-value	0.9477	0.8869	0.9989	0.8588
Kolmogorov-Smirnov P-value	0.8276	0.905	0.9999	0.9354
FEP % Difference	3.29%	0.41%	0.54%	0.39%

3. Simulated and Experimental Results

3.1. Statistical Comparison of GEANT and MCNP Spectra

Two non-parametric distribution-free statistical tests, the Anderson-Darling k-sample test and the Kolmogorov-Smirnov test [13] [14], are employed in comparing the energy spectra datasets from four different source positions obtained from the two Monte Carlo simulations. These tests make no assumptions about the underlying distributions of the datasets compared and are compatible with binned data. An illustrative example of these distributions is shown in Fig. (3) and Fig. (4). The P-values, presented in Table (1), can be interpreted as the likelihood of obtaining a histogram at least as different as the realized histogram if the null hypothesis is true, i.e. the two histograms come from the same dataset. In other words, how likely is the dataset (or a dataset more extreme than the realization), assuming the truth of the null hypothesis. The very high P-values in each case indicate that it is very likely that one can fail to reject the null hypothesis. Thus, the histograms could be obtained in the processing of independent samples taken from one and the same flow of events. These two flows of events are the MCNP and GEANT simulations and they are shown to be statistically indistinguishable in each case considered as we overwhelmingly fail to reject the null hypothesis of these statistical tests with a standard significance level of 0.05. As such, these energy spectra from GEANT and MCNP can be used to derive the detector response curve employed for detector imaging.

3.2. Statistical Comparison of GEANT and Experimental Spectra

3.2.1. Simulated Data Processing

There are two main reasons why one would not expect simulated results and experimental results to be identical. First, in the simulation, the detector was treated as a detector with perfect energy resolution, as the code was written to record exactly the amount of energy

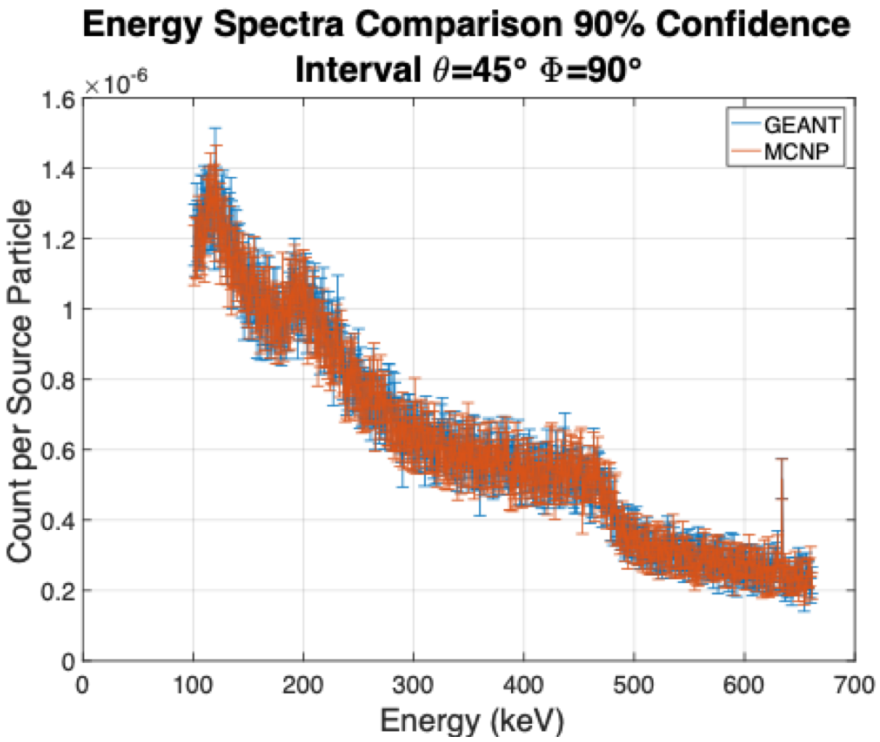

Figure 3: MCNP and GEANT energy spectra for source position (θ,ϕ)=(45°,90°) excluding the FEP for ease of visualization. The 90% confidence interval is shown.

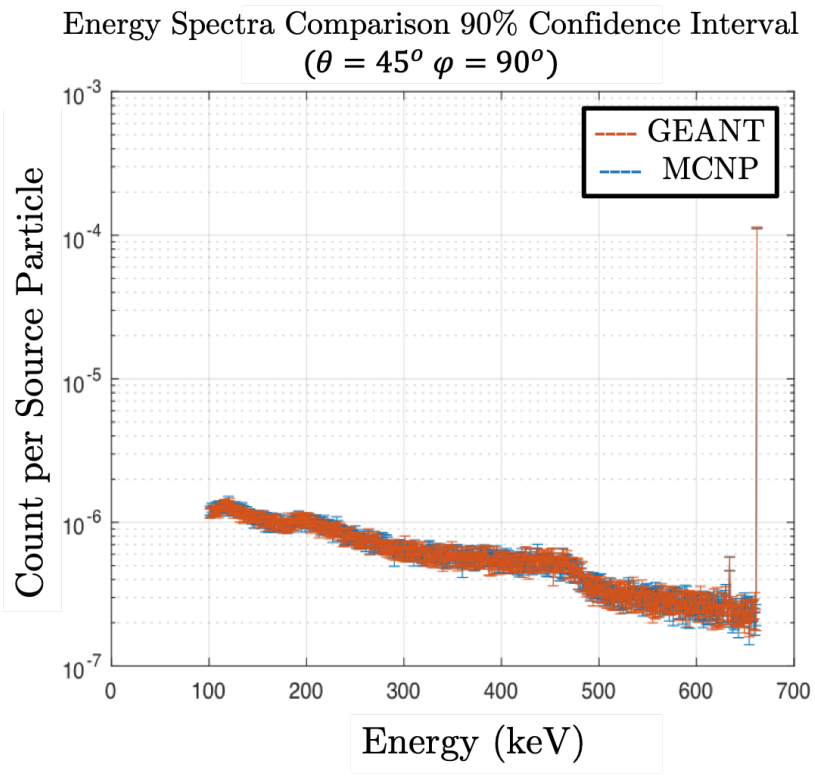

Figure 4: MCNP and GEANT energy spectra visualization for source position (θ,ϕ)=(45°,90°) including the FEP. The 90% confidence interval is shown.

deposited by particles into the detector volume. In comparison, the realistic NaI(Tl) detector has imperfect energy resolution. Second, the simulation does not include Compton scattering contributions from the source by the external lab environment, which consists of a plethora of materials including the base and motor associated directly with the rotation assembly.

The first of these two primary sources of difference is treated via a broadening of the simulated energy spectra. The uncertainty in a realistic NaI(Tl) detector can be approximately modeled as Gaussian in form due to its random nature. [15] This spread was applied to the simulated data via a convolution of the simulated energy spectrum with a Gaussian, the parameters of which are derived from the experimental spectra. This convolution is the area represented by the overlap of two functions as one slides over the entirety of the other, with the two functions being the simulated energy spectra and the Gaussian with experimentally derived standard deviation. [16] Only the central part of the convolution, of range equal to the range of the broadened energy spectrum, is taken as the resulting broadened simulation energy spectrum to be compared with the experimental results. It is recognized that the parameters of the Gaussian with which the energy spectrum should be convolved should vary with energy, as the NaI(Tl) detector resolution is a function of energy. As such, an alternative method of broadening is also employed, for comparison.

This alternative resampling methodology uses a semi-empirical relationship between the calibrated energy bin and the Gaussian standard deviation given by the simple power equation, $\sigma_T = aE^b$, where E in this formula is the energy bin given in MeV. It has been shown that the constants a and b are equal to 0.0302704 and 0.659344 respectively for a 3" $\times$ 3" Heath NaI detector [17] and the constants associated with the detector utilized in this work were found to be 0.0356 and 0.7888 respectively through analysis of the standard deviation obtained as a function of energy using a multinuclide source. Given this energy dependent standard deviation, the simulated counts within each energy bin are resampled from a Gaussian distribution with the proper center and standard deviation.

These three broadening methodologies (convolution with a single Gaussian and resampling with established standard deviation power law constants and derived standard deviation power law constants) are compared in Table (2), in terms of their χ^2 statistic over the entire ^{137}Cs energy spectrum and in Table (3) using only the energy range above 200 keV, where the Compton Scatter contribution is negligible, in the χ^2 calculation. It should be noted that this method of comparison is subject to potential bias due to binning errors, but the effect should be systematic, allowing for valid comparisons of the different broadening methodologies. Table (2) shows that convolution with a Gaussian defined by the experimental ^{137}Cs FEP standard deviation with the simulated data best matches the experiment. Table (3) shows the same result when energy bins 200 keV-1098 keV are considered.

3.2.2. Energy Spectra Comparisons

In Section 3.2.1, comparison of the χ^2 statistic demonstrated that the broadening of the simulated spectrum via convolution with a Gaussian function defined by the experimental ^{137}Cs FEP standard deviation produced superior agreement over the range where simulated

Table 2: χ^2 statistic calculated to compare the entire experimental energy spectrum and the entire broadened simulated energy spectrum for four (θ,ϕ) source positions. Three different broadening methodologies are employed and the Gaussian convolution with ^{137}Cs FEP standard deviation (bold) is shown to be superior on average. The experimental data was collected over a 24h period with a ^{137}Cs source and the simulation was run with 10,000,000 incident 662 keV gamma rays.

Broadening Methodology	(45°,45°)	(90°,45°)	(45°,95°)	(90°,95°)
Gaussian Convolution (^{137}Cs FEP σ)	**39673.85**	**34938.26**	**32149.62**	**38590.50**
Gaussian Resampling with Published Power Law σ	45412.11	42950.78	34100.89	52408.26
Gaussian Resampling with Derived Power Law σ	38057.36	38612.60	39519.21	45867.12

Table 3: χ^2 statistic calculated to compare the 200 keV-1098 keV experimental energy spectrum and the 200 keV-1098 keV broadened simulated energy spectrum for four (θ,ϕ) source positions. Three different broadening methodologies are employed and the convolution of a Gaussian defined by the experimental ^{137}Cs FEP standard deviation with the simulated data (bold) is shown to minimize the error. The experimental data was collected over a 24h period with a ^{137}Cs source and the simulation was run with 10,000,000 incident 662 keV gamma rays.

Broadening Methodology	(45°,45°)	(90°,45°)	(45°,95°)	(90°,95°)
Gaussian Convolution (^{137}Cs FEP σ)	**4174.87**	**2821.95**	**4857.30**	**6229.57**
Gaussian Resampling with Published Power Law σ	5358.53	4411.26	3684.25	9045.32
Gaussian Resampling with Derived Power Law σ	5176.28	5788.53	7597.97	6888.56

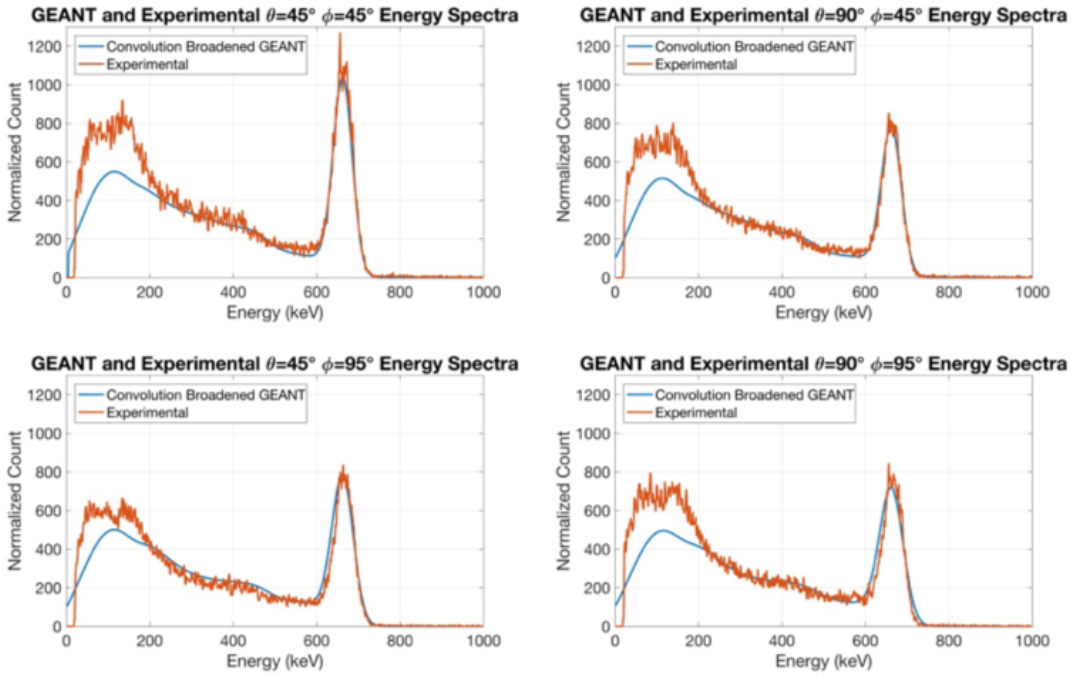

Figure 5: Graphical comparison of broadened (via convolution) GEANT simulation energy spectra and calibrated experimental spectra. The experimental data was collected over a 24h period with a ^{137}Cs source and the simulation was run with 10,000,000 incident 662 keV gamma rays.

Table 4: Non-parametric statistical comparison test results for comparison of broadened GEANT4 and experimental energy spectra for three source positions. The data used in each test represents the count within energy bins 200 keV to 1098 keV for calibrated experimental data and GEANT data broadened via convolution with a Gaussian function defined by the ^{137}Cs FEP standard deviation. All P-values resulting from both the application of the AndersonDarling Test and the KolmogorovSmirnov Test show that the experiment and simulation produce energy spectra that are statistically distinguishable. Thus, the results of experiment and simulation could not have been drawn from the same distribution. The experimental data was collected over a 24h period with a ^{137}Cs source and the simulation was run with 10,000,000 incident 662 keV gamma rays.

Source Position (θ,ϕ)	Anderson-Darling Test P-value	Kolmogorov-Smirnov Test P-value
(45°,45°)	1.26E-15	~ 0
(90°,45°)	3.01E-14	~ 0
(45°,95°)	1.15E-12	~ 0

and experimental data did not diverge (200 keV to 1098 keV). The resulting broadened energy spectra, for four individual source positions, are depicted in Fig. (5) and will be compared statistically in this section via two nonparametric distribution-free statistical tests, the Anderson-Darling k-sample test and the Kolmogorov-Smirnov test. Neither of these tests requires any assumptions about the histograms being compared. The comparison is made between the experimental and simulated energy spectra over the range from 200 keV to 1098 keV (above the range where the distributions tend to diverge). A likely explanation for the lack of agreement at low energies is the choice to exclude the surrounding lab environemt in simulation. This statistical comparison is made using experimental data collected over a 24h period with a ^{137}Cs source and simulated data resulting from a run of 10,000,000 system-incident 662 keV gamma rays in a conical beam configuration. The resulting low (below 0.05) p-values shown in Table (4) indicate that the two distributions are statistically distinguishable and do not agree. Thus, the simulated and experimental energy spectra contain differences that cannot be completely explained by random variation in the datasets. The most likely cause is the choice to exclude the lab environment, from which photons could scatter into the detector, in the simulation. Fortunately, the imaging system is not dependent on perfect agreement throughout the energy spectra. The detector response curves consist of a specific facet of the spectrum acquired as the scatter mask rotates and these DRCs are found to be sufficient for accurate source imaging, as will be shown in Section 5. This facet is either the count of the particles contributing to the FEP or the integral beneath the Compton Continuum. The comparison of these curves derived using the FEP parameter, which is much more critical to source imaging, is considered in the following section.

3.3. Detector Response Curve Derivation

The detector response curves based on the full energy peak (FEP) from experiment and from simulation (broadened via convolution as discussed in the previous section) are processed in directly parallel manners. First, a Gaussian function is fit to the 662 keV FEP in each energy spectrum. Next, the integral underneath each Gaussian distribution is computed. This integral serves as the count associated with that (θ,ϕ) position of the

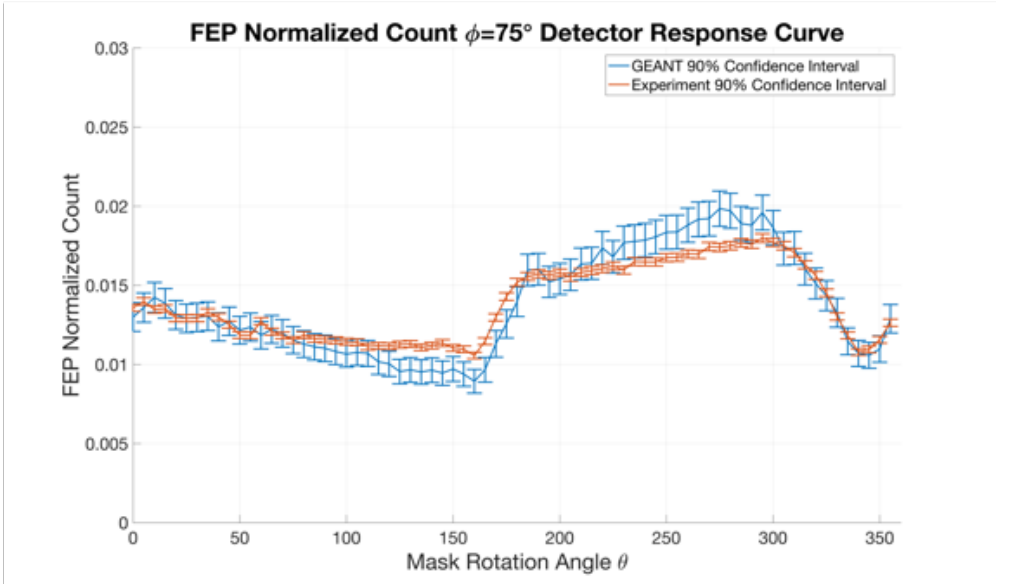

Figure 6: Normalized count (per total count in the detector response curve) that contribute to the FEP for ϕ=75° with θ=0°-355° in increments of 5°. These values correspond to GEANT results with 500,000 source particles for each (θ,ϕ) position and experimental results collected over 24h. The 90% confidence interval is plotted. For each (θ,ϕ) position, the FEP count comes from a broadened energy spectrum (via convolution for GEANT data and inherently for experimental data).

source with respect to the detector. The agreement between curves using this derivation proved dramatically superior to the curve simply taking the exact FEP count derived from the simulation run.

3.4. Detector Response Curve Comparison

The GEANT and experimental detector response curves are compared in a manner analogous to the way that the GEANT and experimental energy spectra were compared previously. These detector response curves represent the integral underneath the FEP for each mask rotation angle $\theta = 5°$ to 360° discretized into 5° increments. Thus, there exist 72 FEP counts representing a unique DRC for each source vector relative to the detector. Each point in each detector response curve is associated with a (θ,ϕ) position of the source relative to the detector, for which 500,000 incident 662 keV gamma rays were simulated. Each experimental detector response curve was collected over a 24h cumulative period. These DRCs required normalization, by the area under each curve, to put the plots on the same scale, as a 24 hour run bears no direct equivalence to a 500,000 particle per position simulation. Two representative DRCs (simulation and experiment) are visualized in Fig. (6) and Fig. (7) for ϕ of 75° and 135° respectively. The 90% confidence intervals are shown in each plot. The excellent agreement in shape should be observed, as will be demonstrated through statistical comparison.

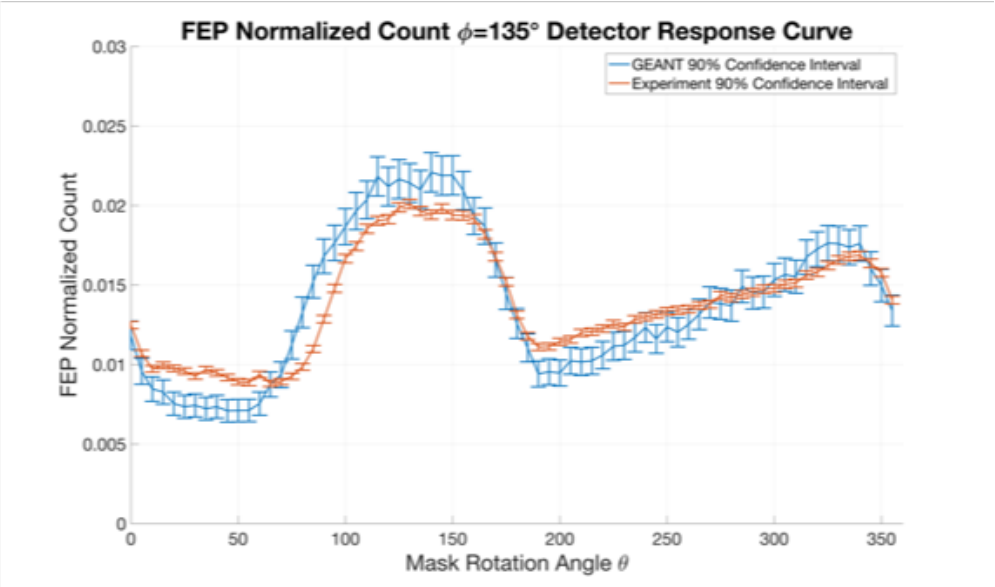

Figure 7: Normalized count (per total count in the detector response curve) that contribute to the FEP for ϕ=135° with θ=0°-355° in increments of 5°. These values correspond to GEANT results with 500,000 source particles for each (θ,ϕ) position and experimental results collected over 24h. The 90% confidence interval is plotted. For each (θ,ϕ) position, the FEP count comes from a broadened energy spectrum (via convolution for GEANT data and inherently for experimental data).

P-values resulting from application of the Kolmogorov-Smirnoff test and the Anderson-Darling test are found in Table (5). The identification relies on differentiating between unique DRCs. As a result, obtaining low p-values does not indicate the identification will perform poorly (as will be seen). Instead these tests provide a reliability metric for the conversion between simulated and experimental DRCs.

Of the 18 curves, the Kolmogoro-Smirnov tests show that all positions except the erroneous 115 results have a p-value above 0.01. Similarly, 11, 7, and 3 curves have a value above 0.10, 0.25, and 0.75 respectively. The Anderson-Darling test has 14, 7, 5, and 1 p-value(s) above 0.01, 0.10, 0.25, and 0.75 respectively.

4. Source Direction Determination Algorithm

With this validated set of simulated detector response curves and a functioning prototype of the RSM system, one can accomplish source localization. The experimentally obtained FEP detector response curve acquired as the RSM/detector assembly is exposed to a radioactive source at an unknown position relative to the detector serves as the algorithm input. To normalize the detector response curve, the FEP count at each point in the experimental curve is divided by the total number of counts in all of the FEP peaks forming the detector response curve. This scales the curve and also makes the normalized detector response curve time-independent. The algorithm output consists of a predicted (θ, ϕ) vector

Table 5: Non-parametric statistical comparison test results for each 10° increment of phi (ϕ= 5°-175°) comparing GEANT4 and experimental DRCs. Each point in each spectrum compared is defined by the number of source particles that contribute to integral beneath a Gaussian curve fitted to the convolution-broadened simulation FEP, out of 500,000 simulated particles per (θ,ϕ) position and experimental FEP associated with a collection period of 24h. At a 0.01 significance level, the bolded P-values indicate that the simulated and experimental results are unlikely to be drawn from the same distribution. ϕ of 115° should be discounted due to an experimental error at this angle. Thus, all curves are shown to agree via the Kolmogorov-Smirnov Test.

Source Position	Anderson-Darling Test P-value	Kolmogoro-Smirnov Test P-value
(0°,5°)	**0.0033463**	0.02186591
(0°,15°)	0.37549	0.3721987
(0°,25°)	0.41592	0.769547
(0°,35°)	0.36133	0.769547
(0°,45°)	0.18449	0.4938319
(0°,55°)	0.060512	0.1316586
(0°,65°)	0.023857	0.1316586
(0°,75°)	0.015072	0.08778698
(0°,85°)	**0.0088668**	0.02186591
(0°,95°)	0.016873	0.03578049
(0°,105°)	0.053276	0.1316586
(0°,115°)	**0.00048322**	**0.000609175**
(0°,125°)	0.022341	0.05686472
(0°,135°)	0.098328	0.2713245
(0°,145°)	0.92734	0.9956171
(0°,155°)	0.17919	0.3721987
(0°,165°)	**0.0054124**	0.03578049
(0°,175°)	0.27495	0.1316586

pointing in the direction of the radioactive source relative to the center of the radiation detector. To produce this output, the algorithm consists of comparison between the input normalized experimental detector response curve and each DRC in the library of broadened, normalized FEP detector response curves obtained from GEANT simulations as discussed in Section 3.3. Normalization of the simulated detector response curves is conducted in the same manner as with the experimental results. The broadening technique of convolution previously applied to the GEANT simulation energy spectra library allows the simulated detector response curve library to be viewed as a static input to the algorithm. This library consists of GEANT FEP detector response curves for each potential discretized source direction. This implies that the library contains one curve for each combination of (θ, ϕ) options, 10° increment of phi (ϕ= 5°- 175°) and 5° increment of theta (θ= 5° - 360°). Each detector response curve consists of a normalized FEP count for each of the 72 discretized rotation angles of the mask, θ = 5° - 360° in increments of 5°. Thus, this library takes the form of a matrix with the following dimensions: (72,18,72) associated with dimensions (source$_\theta$, source$_\phi$, maskRotation$_\theta$). The simple source angle determination algorithm compares the experimental detector response curve against the entire library of simulated detector response curves, accumulating both the simple mean squared error (MSE) and the modal assurance criterion (MAC) in each comparison. The MAC quantifies the degree of proportion between two vectors, with a value near one indicating a strong linear relationship and a value near zero indicating near linear independence between the vectors. [18] Formulae for the MSE and MAC for an experimental curve being compared to a library curve (θ_i, ϕ_j) are given in Eq. (1) and Eq. (2), respectively.

$$ErrorMatrix_{MSE}(i,j) = \sum_{\theta=1}^{72} \frac{[SimLib(i,j,\theta) - ExprCurve(\theta)]^2}{72} \tag{1}$$

$$ErrorMatrix_{MAC}(i,j) = \frac{\left(SimLib(i,j)^T\ ExprCurve\right)^2}{(SimLib(i,j)^T\ ExprCurve)(ExprCurve^T\ ExprCurve)} \tag{2}$$

For a given unknown experimental source position, the MSE and MAC are calculated for this normalized experimental DRC with each normalized simulated library DRC. This forms a (72,18) dimensional matrix indicating how well the experimental DRC agrees with each simulated DRC. The matrix represents an error surface, the minimum MSE (maximum MAC) of which corresponds to the predicted angular position of the experimental source, (θ, ϕ). A representative error surface constructed for experimental source vector (125°,75°) is shown in Fig. (8). The minimum error and, thus, source position predicted by both the MSE and MAC is the correct source vector of (125°,75°). These minimum error DRCs are visualized in Fig. (9).

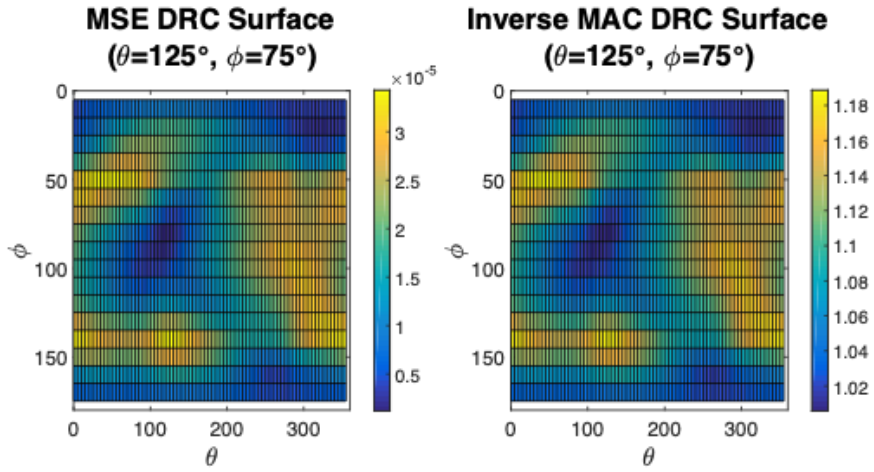

Figure 8: Representative error surface for an input experimental source position. The minimum value in this surface indicates the (θ, ϕ) vector pointing to the predicted source location. Two methods of quantifying the difference between vectors have been applied. The mean squared error and the modal assurance criterion are shown to predict the same source location.

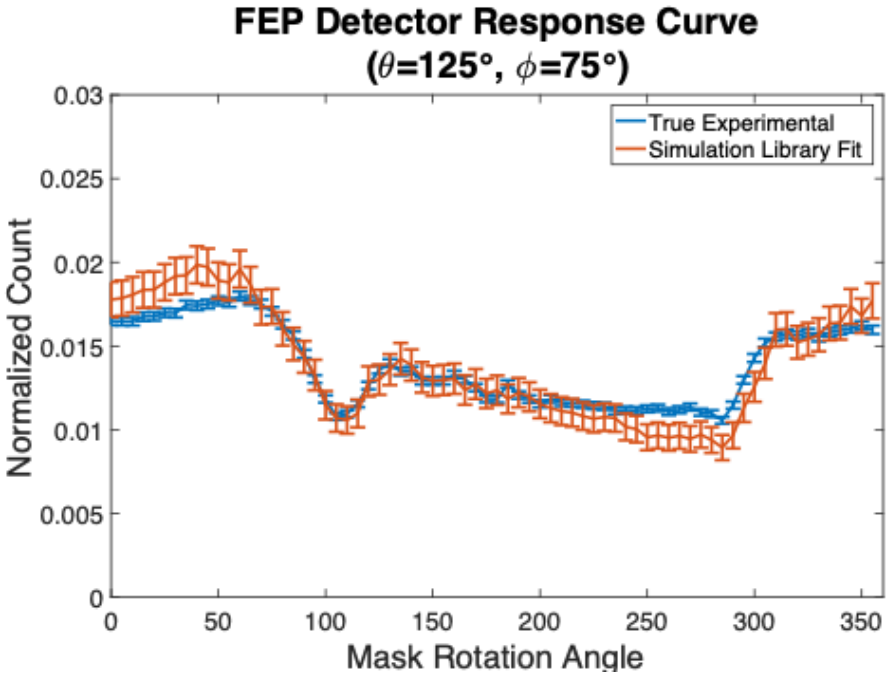

Figure 9: Unknown experimental detector response curve is graphed alongside its predicted best matching simulated library detector response curve (minimum in Fig. (8)). This predicted source vector is correct in that the experimental source was located at (θ,ϕ)= (125°,75°). It is the close agreement between these two curves that allows source position determination.

5. Source Position Determination Accuracy

The simple algorithm detailed in Section 4 works remarkably well. To test its functionality, experimental detector response curves for each potential source position (θ, ϕ) combination were fed into the algorithm. The algorithm completed this set of 1296 source direction determinations in less than a second on a standard laptop, implying the algorithm computational time is of negligible concern. The resulting errors in the predicted (θ, ϕ) source directions are shown in Table (6), for each of the true experimental source positions. The average (absolute value) errors of both the azimuthal angle θ and polar angle ϕ are less than 5° (average error being 4° in θ and 3° in ϕ). This is a good, although potentially misleading, result as the resolution in the library for θ is 5° and the resolution in the library for ϕ is 10°.

It must be noted that the set of input experimental detector response curves consists of 18 unique experiments. The complete set of 1296 input curves can be obtained from these 18 curves because a change in the source position associated with a different θ angle for the same ϕ angle simply represents a shift of the (θ, ϕ) = (0°, ϕ) curve by the angle associated with the experimental position in θ. Put in a different way, different source positions with the same ϕ simply represent different starting points of tracking of the rotation angle of the mask in θ. Thus, the curve shapes are identical, but shifted in their position along the θ axis. Due to this feature of the experimental input dataset, all input curves which represent positions with the same ϕ polar angle will have the same detector response curve shape, with the offset indicating the different θ azimuthal angle of the source. Thus, when the algorithm is applied to this set of curves, if the ϕ angle is predicted correctly, but there is an error in the θ angle predicted, this same error will occur with all θ angle experimental positions. For this reason, it is complete to present source direction prediction errors for only (θ, ϕ) = (90°, ϕ) as was done in Table (6). All source position comparison results can be derived from the comparison presented in this table.

All tests assumed the presence of a source experimentally. In practice, a source's presence would be deduced by the detector registering a given number of counts in a given time (e.g. 100 counts/second) above 200 keV. Once this threshold has been reached, the best-fit library identification will attempt to determine its direction. When the number of counts is near the threshold, the algorithm will choose the curve(s), which most closely resemble the measured data. As the number of counts increases, the identification accuracy and signal trait distinguishability will also increase. If no source is present, either the threshold counts will not be achieved or the reported fit quality will be poor.

A critical part of the imaging ability is derived from the relative positions and magnitudes of the maximum and minimum counts in the DRC. To roughly estimate the degradation of the imaging ability with decreasing source activity, the minimum number of total source mask-incident particles that prevent the overlap of the confidence intervals of the DRC maximum and minimum are computed. It is found from the simulation that a 5×10^5 mask-incident particle count per θ discretization can be reduced by a factor of 1/100 with response curve overlap on only the two most extreme ϕ angles. Given this reduced count, and considering if the θ discretization is reduced from 5° to 10°, the new total number of

Table 6: Source direction determination error utilizing a simulated library with resolution of 10° in phi (ϕ= 5°- 175°) and 5° in theta (θ= 5° - 360°). Results correspond to the minimum mean squared error or modal assurance criterion of the experimental curve with the simulation library matrix of DRCs (each criterion produced identical results in all cases). As discussed previously, the large error in 115° is a consequence of an experimental disruption occurring during that run. All source position comparison results can be derived from the comparison presented in this table.

ϕ	θ error	ϕ error
5°	10°	0°
15°	5°	0°
25°	5°	0°
35°	0°	0°
45°	0°	0°
55°	0°	0°
65°	10°	10°
75°	0°	0°
85°	0°	0°
95°	5°	10°
105°	0°	0°
115°	140°	100°
125°	5°	10°
135°	5°	10°
145°	5°	0°
155°	0°	0°
165°	0°	10°
175°	20°	0°

mask-incident particles per revolution required for discrimination is 1.8×10^5 photons. This value provides a rough estimate of minimum incident photons required for accurate location at this resolution. A parametric quantification study is included by Olesen et. al. as part of an optimized mask design; that work provides a similar estimate and discussion of the number of particles required to accurately determine the source position [12].

6. Conclusion

This analysis has demonstrated the feasibility of the use of a rotating scatter mask assembly, consisting of a particularly designed mask surrounding a single NaI detector, as a source location determination system. It is shown that not only does one obtain unique detector response curves (DRCs) for each source position in the nearly 4π field of view via both simulation and experiment, but that in the vast majority of cases, these experimentally and simulation derived DRC are statistically indistinguishable. As such, this validated simulation can be used to efficiently derive a library of DRCs. It has also been shown that this library can then serve as input to an imaging algorithm to determine the position of a source relative to a detector when only the experimental DRC is known. This work empowers

future research in fielding a RSM system for gamma source localization. Additionally, the experimental validation, performed here, of the DRCs obtained from MCNP and GEANT4 permits future rapid exploration of improved mask designs through simulation to increase the identification accuracy, decrease the identification time, and to permit multiple source detection and imaging.

7. Acknowledgment

The authors would to thank Maj. Christopher Charles for construction and testing of the initial additive manufactured mask. We also thank Dr. David Wehe of the University of Michigan for loan of the drive assembly used in the RSM experiments.

The views expressed in this article are those of the authors and do not necessarily reflect the official policy or position of the United States Air Force, the Department of Defense, or the United States Government. This research was supported in part by the Defense Threat Reduction Agency.

References

[1] Management of Disused Sealed Radioactive Sources, no. NW-T-1.3 in Nuclear Energy Series, INTERNATIONAL ATOMIC ENERGY AGENCY, Vienna, 2014.
URL https://www.iaea.org/publications/10582/management-of-disused-sealed-radioactive-sources

[2] I. Tsilikis, I. Pantos, I. Zouliati, A. Koutras, G. Kalinterakis, A. Syllaios, Radiological risks from potential exposure of the population to radiation from orphan radioactive sources, Health Physics 116 (5) (2019) 715719. doi:10.1097/hp.0000000000001003.

[3] R. Wurtz, K. . Ziock, L. Fabris, R. Graham, Comparing imaging and non-imaging techniques for reducing background clutter and resolving distant point sources, in: IEEE Nuclear Science Symposium Conference Record, 2005, Vol. 1, 2005, pp. 338–342. doi:10.1109/NSSMIC.2005.1596266.

[4] K. P. Ziock, J. W. Collins, L. Fabris, S. Gallagher, B. K. P. Horn, R. C. Lanza, N. W. Madden, Source-search sensitivity of a large-area, coded-aperture, gamma-ray imager, IEEE Transactions on Nuclear Science 53 (3) (2006) 1614–1621. doi:10.1109/TNS.2006.875285.

[5] A. L. Hutcheson, B. F. Phlips, E. A. Wulf, L. J. Mitchell, W. N. Johnson, B. E. Leas, Maritime detection of radiological/nuclear threats with hybrid imaging system, in: 2013 IEEE International Conference on Technologies for Homeland Security (HST), 2013, pp. 360–363. doi:10.1109/THS.2013.6699030.

[6] G. H. Nakano, L. F. Chase, J. R. Kilner, W. G. Sandie, G. J. Fishman, W. S. Paciesas, R. E. Lingenfelter, S. E. Woosley, Songs - a high resolution imaging gamma-ray spectrometer for the space station, EUV, X-Ray, and Gamma-Ray Instrumentation for Astronomy and Atomic Physics-doi:10.1117/12.962575.

[7] B. R. Kowash, Rotating modulation imager for the orphan source search problem, Ph.D. thesis (2008).

[8] Specifications of polaris-h gamma-ray imaging spectrometer (2017).
URL www.valitustech.com/Old-Site/files/theme/polarishspecs.pdf

[9] D. Longford, M. Kiser, E. Hull, P. Aspetti, E. Santoni, Gegi gamma-ray imaging spectrometer: redefining stand-off radiation detection of special nuclear material.

[10] D. E. Holland, J. E. Bevins, L. W. Burggraf, B. E. ODay, Rotating scatter mask optimization for gamma source direction identification, Nuclear Instruments and Methods in Physics Research Section A: Accelerators, Spectrometers, Detectors and Associated Equipment 901 (2018) 104 – 111. doi:https://doi.org/10.1016/j.nima.2018.05.037.
URL http://www.sciencedirect.com/science/article/pii/S0168900218306429

[11] J. G. M. FitzGerald, A rotating scatter mask for inexpensive gamma-ray imaging in orphan source search: Simulation results, IEEE Transactions on Nuclear Science 62 (1) (2015) 340–348. doi:10.1109/TNS.2014.2379332.

[12] R. J. Olesen, B. E. ODay, D. E. Holland, L. W. Burggraf, J. E. Bevins, Characterization of novel rotating scatter mask designs for gamma direction identification, Nuclear Instruments and Methods in Physics Research Section A: Accelerators, Spectrometers, Detectors and Associated Equipment- doi:https://doi.org/10.1016/j.nima.2018.09.067.
URL http://www.sciencedirect.com/science/article/pii/S0168900218312117

[13] S. Bityukov, A. Maksimushkina, V. Smirnova, Comparison of histograms in physical research, Nuclear Energy and Technology 2 (2) (2016) 108 – 113. doi:https://doi.org/10.1016/j.nucet.2016.05.007.
URL http://www.sciencedirect.com/science/article/pii/S2452303816300437

[14] S. Engmann, D. Cousineau, Comparing distributions: the two-sample andersondarling test as an alternative to the kolmogorovsmirnov test, Journal of Applied Quantitative Methods 6 (2011) 1–17.

[15] G. F. Knoll, Radiation Detection and Measurement, 4th Edition, John Wiley Sons, 2012.

[16] H. H. Barrett, W. Swindell, 3 - theory of random processes, in: H. H. Barrett, W. Swindell (Eds.), Radiological Imaging, Academic Press, San Diego, 1981, pp. 62 – 116. doi:https://doi.org/10.1016/B978-0-08-057230-7.50010-X.
URL http://www.sciencedirect.com/science/article/pii/B978008057230750010X

[17] R. P. Gardner, A. Sood, A monte carlo simulation approach for generating nai detector response functions (drfs) that accounts for non-linearity and variable flat continua, Nuclear Instruments and Methods in Physics Research Section B: Beam Interactions with Materials and Atoms 213 (2004) 87 – 99, 5th Topical Meeting on Industrial Radiation and Radioisotope Measurement Applications. doi:https://doi.org/10.1016/S0168-583X(03)01539-8.
URL http://www.sciencedirect.com/science/article/pii/S0168583X03015398

[18] V. Rotondella, A. Merulla, A. Baldini, S. Mantovani, Dynamic modal correlation of an automotive rear subframe, with particular reference to the modelling of welded joints, Advances in Acoustics and Vibration 2017. doi:10.1155/2017/8572674.